

# On the Performance of a Real-Time Electron Radiation Belt Specification Model

Frances A Staples<sup>1</sup>, Adam C Kellerman<sup>1</sup>, and Janet C. Green<sup>2</sup>

<sup>1</sup>University of California Los Angeles

<sup>2</sup>Space Hazards Applications, LLC

April 08, 2024

## Abstract

Maintaining accurate real-time hindcast and forecast specification of the radiation environment is essential for operators to monitor and mitigate the effects of hazardous radiation on satellite components. The Radiation Belt Forecasting Model and Framework (RBFMF) provides real-time forecasts and hindcasts of the electron radiation belt environment, which are used as inputs for the Satellite Charging Assessment Tool (SatCAT). We evaluated the long-term statistical error and bias of the RBFMF by comparing the 10-hour hindcast of electron phase space densities (PSD) to a multi-mission dataset of PSD observations. We found that, between the years 2016-2018, the RBFMF reproduced the radiation belt environment to within a factor of 1.5. While the error and bias of assimilated observations were found to influence the error and bias of the hindcast, data assimilation resulted in more accurate specification of the radiation belt state than real-time Van Allen Probe observations alone. Furthermore, when real time Van Allen Probe observations were no longer available, the hindcast errors increased by an order of magnitude. This highlights two needs; (i) the development of physics-based modelling incorporated into this framework, and (ii) the need for real-time observations which span the entire outer radiation belt.

## Hosted file

Validation paper\_v2.docx available at <https://authorea.com/users/548802/articles/742326-on-the-performance-of-a-real-time-electron-radiation-belt-specification-model>

# On the Performance of a Real-Time Electron Radiation Belt Specification Model

Frances Staples<sup>1</sup>, Adam Kellerman<sup>1</sup>, Janet Green<sup>2</sup>

<sup>1</sup>Department of Atmospheric & Oceanic Sciences, University of California, Los Angeles, Los Angeles, CA, USA.

<sup>2</sup>Space Hazards Applications, LLC.

Corresponding Author: Frances Staples (fastaples@atmos.ucla.edu)

## Key Points

- Real-time data-assimilative hindcasts of the outer electron radiation belt were accurate to within a factor of 1.5. Data assimilation substantially improved the error and bias of radiation belt specification but strongly influenced hindcast error and bias.
- Improved physics-based modeling and continuous real-time observations through the outer radiation belt are needed for accurate hindcasts.

## 16 Abstract

17 Maintaining accurate real-time hindcast and forecast specification of the radiation environment  
18 is essential for operators to monitor and mitigate the effects of hazardous radiation on satellite  
19 components. The Radiation Belt Forecasting Model and Framework (RBFMF) provides real-time  
20 forecasts and hindcasts of the electron radiation belt environment, which are used as inputs for  
21 the Satellite Charging Assessment Tool (SatCAT). We evaluated the long-term statistical error  
22 and bias of the RBFMF by comparing the 10-hour hindcast of electron phase space densities  
23 (PSD) to a multi-mission dataset of PSD observations. We found that, between the years 2016-  
24 2018, the RBFMF reproduced the radiation belt environment to within a factor of 1.5. While the  
25 error and bias of assimilated observations were found to influence the error and bias of the  
26 hindcast, data assimilation resulted in more accurate specification of the radiation belt state  
27 than real-time Van Allen Probe observations alone. Furthermore, when real time Van Allen Probe  
28 observations were no longer available, the hindcast errors increased by an order of magnitude.  
29 This highlights two needs; (i) the development of physics-based modelling incorporated into this  
30 framework, and (ii) the need for real-time observations which span the entire outer radiation  
31 belt.

## 32 Plain Language Summary

33 It is important to accurately predict and monitor the radiation levels in space to safeguard  
34 satellites from potential damage. This paper introduces a model called the Radiation Belt  
35 Forecasting Model and Framework (RBFMF), which provides real-time forecasts and historical  
36 data (hindcasts) of radiation levels. To test the model's accuracy, we compared its predictions to  
37 actual observations from satellites between 2016 and 2018. We found that generally, the  
38 model's predictions of the outer radiation belt were within 1.5 times of the actual  
39 measurements. Additionally, we discovered that incorporating both real-time satellite  
40 observations and physics-based simulation improved prediction accuracy compared to relying  
41 solely on either method. However, we noticed a significant increase in prediction errors when  
42 real-time observations through the heart of the Van Allen radiation belt were unavailable. This  
43 underscores the importance of enhancing the model with physics-based modeling and ensuring  
44 continuous real-time observations of radiation levels in space.

## 45 1 Introduction

46 The variability of the near-Earth radiation environment poses a serious hazard to  
47 telecommunications, navigational, and defense satellites which orbit through these regions. A  
48 key effect of spacecraft exposure to radiation is internal charging, where high energy electrons  
49 penetrate the surface shielding of a satellite and deposit charge into dielectric materials such as  
50 circuit boards or cable insulators, and on ungrounded material such as spot shields or connector  
51 contacts (e.g., Fennell et al., 2001; Lohmeyer et al., 2015). The accumulated charging eventually  
52 results in electrostatic discharges, which is one of the known causes of “satellite anomalies”.  
53 Anomalies range in effect from more frequent temporary errors in non-critical systems to rare  
54 but catastrophic hardware damage and complete mission failure (Galvan et al., 2014) and can be  
55 instigated by a number of issues, such as command errors, manufacture flaws, and  
56 environmental exposures. Of all space environment effects on satellites, electrostatic discharges  
57 from internal charging have been reported to cause the most anomalies (Green et al., 2017;  
58 Koons et al., 1999).

59 Improved on-orbit anomaly detection tools have been cited by satellite operators as an  
60 industrial need for operators to easily and quickly attribute anomalies to space weather effects  
61 (Green et al., 2017). To attribute satellite anomalies to internal charging of equipment requires  
62 forensic reconstruction of the radiation environment and modelling of charge accumulation on  
63 component hardware, such as satellite shielding materials, for defined orbits (LEO, MEO, GEO).  
64 The Satellite Charging Assessment Tool (SatCAT) is one such tool which allows users to monitor  
65 the real time and long-term effects of internal charging due to fluence of radiation belt  
66 electrons. This paper will evaluate the Radiation Belt Forecasting Model and Framework (RBFMF)  
67 which SatCAT uses to specify the radiation environment both retrospectively and in real-time.

68 Several models have been developed to model the near-Earth radiation environment based  
69 upon the Van Allen radiation belt response to solar wind parameters and/or geomagnetic  
70 indices. These models usually fall within three categories; empirically based analytical  
71 descriptions (e.g., X. Li, 2004; Nagai, 1988; Roeder et al., 2005; Turner & Li, 2011), physics-based  
72 models (e.g., Horne et al., 2013; Subbotin & Shprits, 2009), and machine learning models (e.g.,

73 Boyd et al., 2023; Chen et al., 2019; Wei et al., 2018). Statistical approaches to modelling the  
74 radiation belt have shown success at identifying the key variables which influence radiation belt  
75 flux on different timescales. However, statistical approaches do not capture some extreme  
76 events, and could be flawed if they cannot reflect the non-linear relationship between input  
77 variables are output electron fluxes. While physics-based modelling allows the study of relative  
78 contributions of complex acceleration and loss mechanisms in the outer radiation belt, the  
79 computational power required to accurately model the interconnected magnetospheric system  
80 on an hourly basis provides a significant challenge. Machine learning models have predicted  
81 ultra-relativistic electron fluxes with high efficacy but show less accuracy at predicting lower  
82 energy fluxes (Camporeale, 2019; Shin et al., 2016) but, similarly to statistical modelling, could  
83 have limited capabilities for extreme event which are out of sample to training data.

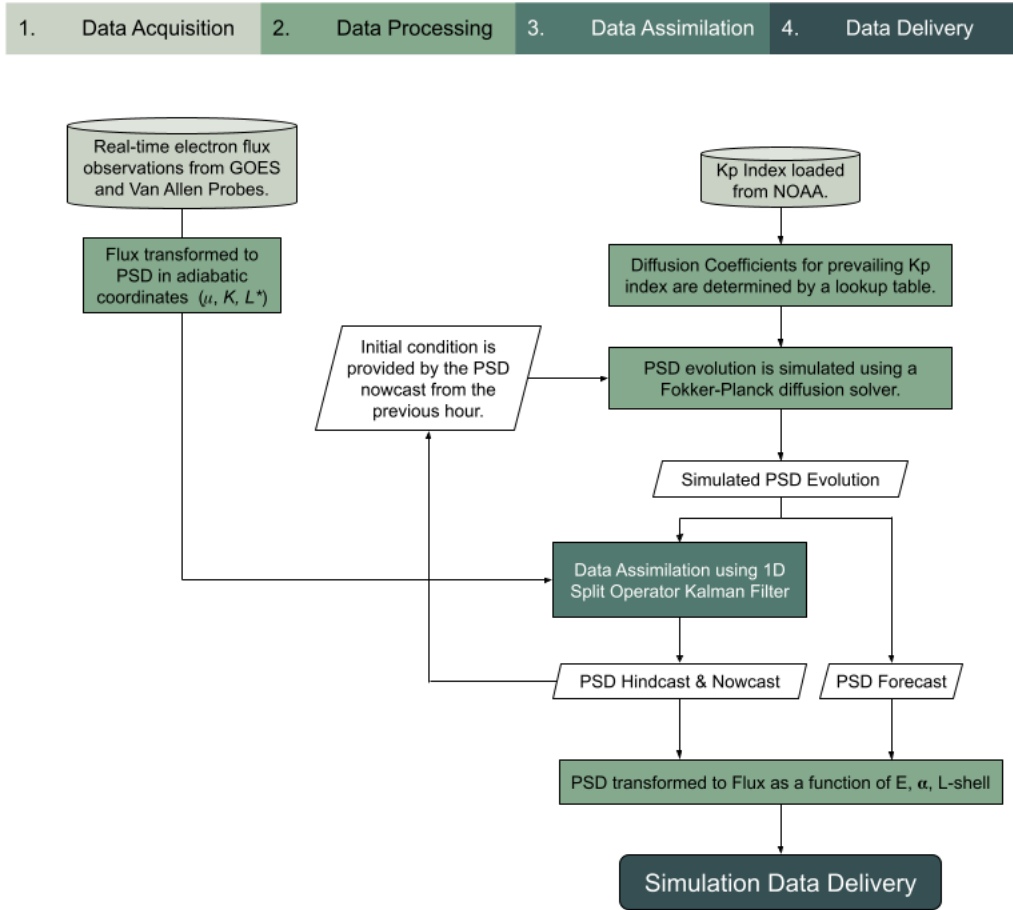
84 By combining physics-based modelling with data assimilative techniques, RBFMF provides a  
85 lightweight and robust tool for real time radiation belt forecasting. This framework uses 1D  
86 Kalman filtering technique which has previously been shown through event-based studies to be  
87 a successful tool for reproducing the radiation belts (e.g., Coleman et al., 2018; Daae et al., 2011;  
88 Kellerman et al., 2014). This work will investigate the performance of this forecasting  
89 methodology by completing a detailed statistical evaluation of RBFMF over archived multi-year  
90 dataset of hindcasts. We aim to assess how data assimilation affects the error and bias of  
91 radiation belt forecasts, and the influence of variable geomagnetic conditions. In this way, we  
92 will identify how the RBFMF may be adapted in the future for improved hindcast reliability.

## 93 **2 Radiation Belt Forecasting Model and Framework**

94 The radiation belt forecast framework (RBFMF) is designed to combine physics-based modelling  
95 with data assimilative techniques to provide forecasts, nowcasts, and hindcasts of the radiation  
96 environment in real-time. This framework is based upon an existing data assimilative models  
97 developed by Kellerman et al. (2014) and Shprits et al. (2013), and has been further developed to  
98 provide a more robust forecasting infrastructure which provides data products which are  
99 integrated into the SatCAT tool. The implementation of this framework is summarized in Figure  
100 1.

**Radiation Belt Forecasting Model and Framework**

Each hour these steps are iterated to provide an updated hindcast, nowcast, and forecast.



101

102 **Figure 1** Flow chart summarizing the steps completed each hour in the RBFMF.

103 *Diffusive Modelling*

104 Radiation belt diffusion is modelled through implementation of the 3-D Fokker-Plank diffusion  
 105 equation for radiation, Equation 1, (Roederer, 1970; Schulz & Lanzerotti, 1974; Walt, 1994).

106

$$\frac{\partial f}{\partial t} = \sum_{i,j} \frac{\partial}{\partial J_i} \left( D_{J_i J_j} \frac{\partial f}{\partial J_j} \right) - Losses \quad \text{Equation 1}$$

107 Where  $f$  is the phase averaged electron phase space density (PSD),  $J_i, J_j$ , represent the first,  
 108 second, and third adiabatic invariants of adiabatic motion ( $\mu, J, \Phi$  respectively), and diffusion

109 coefficients  $D_{J_i J_j} = \langle \Delta J_i \Delta J_j \rangle / (2\Delta t)$  which denote the scattering rates ( $D_{\mu\mu}, D_{JJ}, D_{\Phi\Phi}$ ). In this paper  
 110 we will use  $K$  ( $\propto J$  assuming  $\mu$  is conserved) as the second adiabatic invariant and  $L^*$  ( $\propto 1/\Phi$ ) as  
 111 the third adiabatic invariant (noting that  $L^* = L$  in a dipolar magnetic field). The Versatile Electron  
 112 Radiation Belt (VERB) code (Subbotin & Shprits, 2009) is used to implement a solution to this  
 113 equation using precomputed diffusion coefficients.

#### 114 *Diffusion Coefficients*

115 By precomputing diffusion matrices, the diffusion equation can be solved quickly at each time  
 116 step by selecting diffusion coefficients for the prevailing  $Kp$  level. Mixed local diffusion terms are  
 117 excluded, which enables larger grid steps. Three types of waves were used to derive the  
 118 diffusion coefficient matrices; ULF waves (Brautigam & Albert, 2000), lower-band chorus (W. Li et  
 119 al., 2007; Shprits et al., 2007) and plasmaspheric hiss (Spasojevic et al., 2015). The plasma density  
 120 was obtained from (Sheeley et al., 2001) for diffusion coefficient computation. The diffusion  
 121 coefficients were computed using the Full Diffusion Code at UCLA.

#### 122 *Initial and Boundary Conditions*

123 Diffusion is solved for a dipolar magnetic field with a grid covering L-shells 1 to 7, energies 10  
 124 keV to 10 MeV, and pitch angles  $0.3^\circ - 89.7^\circ$ . The upper boundary condition in energy is a  
 125 Dirichlet boundary with constant  $f = 0$ , the lower-boundary condition is also Dirichlet for each  
 126 time step, although updated by assimilation. The lower boundary condition in pitch angle is a  
 127 Neumann boundary  $\partial f / \partial \alpha = 0$ , to allow for both weak and strong diffusion effects to be  
 128 simulated. The upper boundary condition in  $L$  utilizes both Dirichlet and Neumann boundaries,  
 129 depending on the last closed drift shell (LCDS) derived from Tsyganenko (1989) with a centered  
 130 dipole (see Kellerman, 2018). The lower boundary in  $L$  is a Dirichlet boundary, with  $f = 0$  at  $L_{min}$ ,  
 131 representing loss to the atmosphere.

132 The model was initialized through the average PSD observed by spacecraft from the previous  
 133 month. For each additional forecast going forward through several years, the initial condition of  
 134 each time step is set to the nowcast simulated for the previous hour.

135 *Data Assimilation*

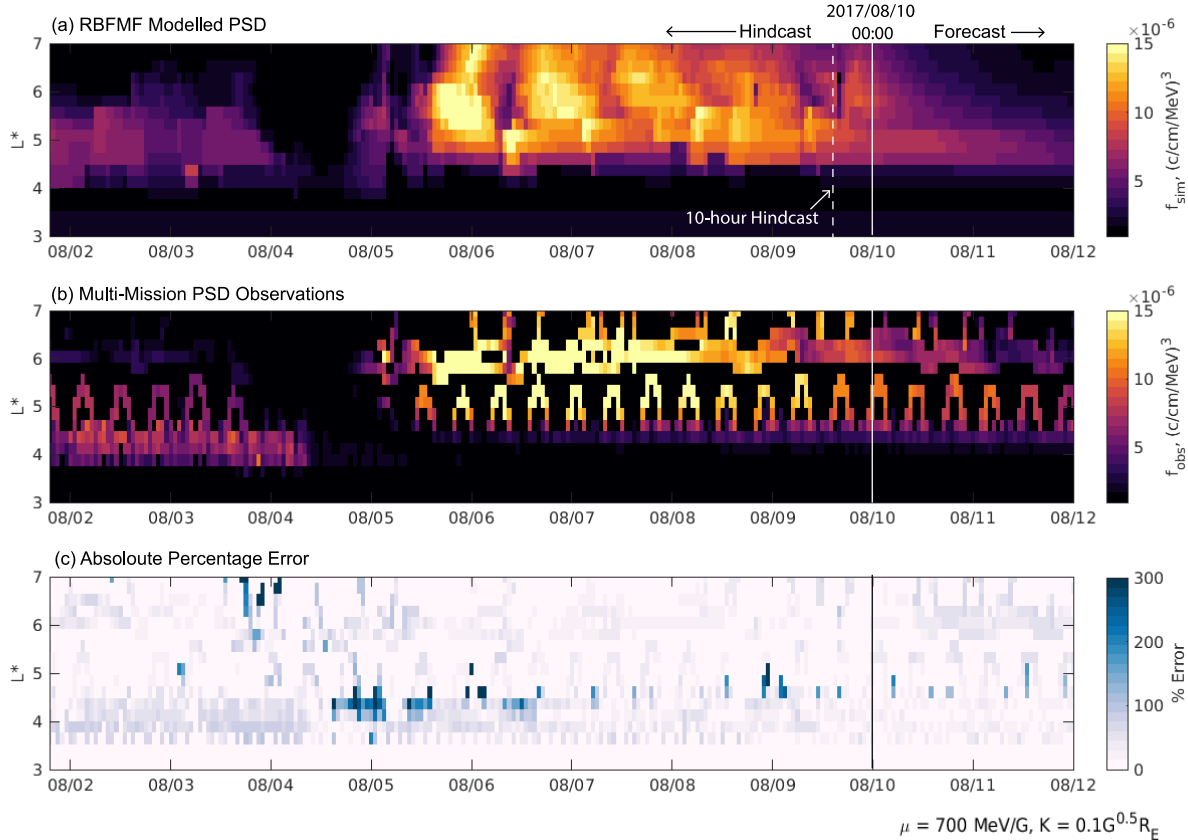
136 Data assimilation uses filtering algorithms to estimate the state of a system using joint  
137 probability distributions from a simulated system and sparsely observed data. The Kalman Filter  
138 (Kalman, 1960) is a widely used data assimilation algorithm which estimates the system state by  
139 minimizing the mean square errors of the simulated state variables and observed state variables.  
140 Readers are referred to past works for detailed descriptions the Kalman filter to radiation belt  
141 analysis (e.g., Kondrashov et al., 2007; Naehr & Toffoletto, 2005; Ni et al., 2009; Shprits et al.,  
142 2007). Because the computational requirements of a 3D Kalman filter are very large, making it  
143 impractical for real time applications, the RBFMF instead employs a one-dimensional split-  
144 operator Kalman filter. This methodology has been validated in a synthetic-forecast analysis over  
145 multiple years (Kellerman, 2018). Due to several unknown errors in the model and real-time  
146 observational datasets, the errors were set equal for data and model.

147 **2.1 Observations**

148 Figure 2 shows how the modelled radiation belt PSD compares to the multi-mission PSD  
149 observations (described further in Section 3). The nowcast time is indicated in Figure 2 by the  
150 white line, with the preceding eight days showing hindcast PSD, and the following two days  
151 show the PSD forecast. By comparing the modelled PSD in Figure 2a to the measured PSD in  
152 Figure 2b, we can see that the RBFMF is highly successful at reproducing the structure and  
153 dynamical evolution of the radiation belt in this example. The magnitude of the radiation belt  
154 flux is well captured overall, although when the observed PSD became enhanced up to  $\sim 15 \times$   
155  $10^{-5} \text{ (c/cm/MeV)}^3$  at  $5 < L^* < 6$  between 6-9<sup>th</sup> August, the hindcast PSD appeared to be slightly  
156 underestimated. Figure 2c shows that the percentage error was  $< 100\%$  for most of the interval  
157 (i.e., PSD was estimated within a factor of 1 during the interval), but became largest ( $> 200\%$ )  
158 near the outer boundary ( $L^* > 6$ ) as electrons were lost on 3<sup>rd</sup> August, and along the inner edge  
159 of the radiation belt ( $4 < L^* < 5$ ) during the enhancement between 4<sup>th</sup> to 7<sup>th</sup> August.

160 While the interval in Figure 2 appears to show that the RBFMF is a good representation of the  
161 outer radiation belt, we must quantitatively evaluate the performance of the model to determine if  
162 it is accurate over long time periods, and identify when the simulation is inaccurate so that it can

163 be improved. We will test the RBFMF against the observed state of the electron radiation belt for  
 164 two time periods between 2016 - 2018 and between 2019 - 2020. The key difference between  
 165 these years is that between 2016-2018 both GOES and Van Allen Probe data were assimilated  
 166 into the hindcast in real time, whereas from 2019 onwards, only GOES data was assimilated in  
 167 real time.



168

169 **Figure 2** The simulated state of the radiation belt,  $f_{sim}$ , at 00 UT on 10<sup>th</sup> August 2017 is  
 170 displayed in panel (a) as a function of  $L^*$  over time, for  $\mu = 700 \text{ MeV/G}$  and  $K = 0.1 \text{ G}^{0.5} R_E$ .  
 171 Panel (b) shows corresponding PSD observations,  $f_{obs}$ , taken by multiple missions. Panel  
 172 (c) shows the absolute percentage error of the simulated PSD:  $|f_{obs} - f_{sim}| / f_{sim} \times 100$ .

### 173 3 Validation Method

174 In this analysis, the RBFMF will be validated against a multi-mission dataset of radiation belt  
 175 observations (described in Section 3.1), which serves as the ‘true’ state of the radiation belt. The  
 176 error and bias of the radiation belt hindcast of electron phase space density (PSD) is analyzed in

177 adiabatic coordinates. To do this, the observed PSD (described in Sections 3.1) is converted onto  
 178 the same resolution coordinate grid as the simulated PSD by interpolating across the first and  
 179 second adiabatic invariants,  $\mu$  and  $K$ , then averaging PSD into  $L^*$  bins on an hourly basis. The  
 180 quotient ( $Q_i = f_{sim}/f_{obs}$ ) of each simulation data point can then be determined if there is a  
 181 corresponding PSD observation.

182 The statistical error and bias of the 10-hour hindcast is calculated between January 2016 –  
 183 October 2019 and between March 2019 – December 2020. Special focus is given to the 10-hour  
 184 hindcast (dashed line, Figure 2a) because this is the most frequently used by satellite operators  
 185 for anomaly attribution. Error and bias are quantified using symmetric metrics described by  
 186 Morley et al. (2018), which account for variable electron PSD magnitudes. The median symmetric  
 187 accuracy (MSA) is described in Equation 2 and the symmetric signed percentage bias (SSPB) is  
 188 described in Equation 3, where  $M()$  symbolizes the median calculation. In this scheme, the MSA  
 189 is small if simulation errors are low,  $SSPB < 0$  if the hindcast is biased towards underprediction  
 190 of PSD, and  $SSPB > 0$  if the hindcast is biased towards overprediction of PSD.

$$MSA = 100 (\exp ( M(| \log_e(Q_i) |) ) - 1 ) \quad \text{Equation 2}$$

191

$$SSPB = 100 \operatorname{sgn}(M(\log_e(Q_i)))(\exp ( M(| \log_e(Q_i) |) ) - 1 ) \quad \text{Equation 3}$$

### 192 3.1 Multi-Mission PSD Observations

193 PSD observations are taken from 32 individual satellites which are part of 5 different scientific  
 194 missions and hosted payloads (see Staples et al., 2022; Staples et al., 2023 for usage of this  
 195 dataset):

- 196 • Van Allen Probe Magnetic Electron Ion Spectrometer (MagEIS) and Relativistic Electron-  
 197 Proton Telescope (REPT) instruments (Baker et al., 2014; Blake et al., 2014).

- 198 • GOES 13 and 15 (Geostationary Operational Environmental Satellite) Magnetospheric  
199 Electron Detector (MAGED) Energetic Proton, Electron, and Alpha Detector (EPEAD)  
200 (Rodriguez, 2014a, 2014b; Sillanpää et al., 2017).
- 201 • GPS (Global Positioning System) Navstar Combined X-ray dosimeter (CXD) (Morley et al.,  
202 2017; Tuszewski et al., 2004).
- 203 • THEMIS (Time History of Events and Macroscale Interactions during Substorms)  
204 Electrostatic Analyzer (ESA) and Solid-State Telescope (SST) (Angelopoulos, 2008;  
205 Angelopoulos et al., 2008; McFadden et al., 2008).
- 206 • MMS (Magnetospheric Multiscale) Fly's Eye Electron Proton Spectrometer (FEEPS) (Blake  
207 et al., 2016; Burch et al., 2016).

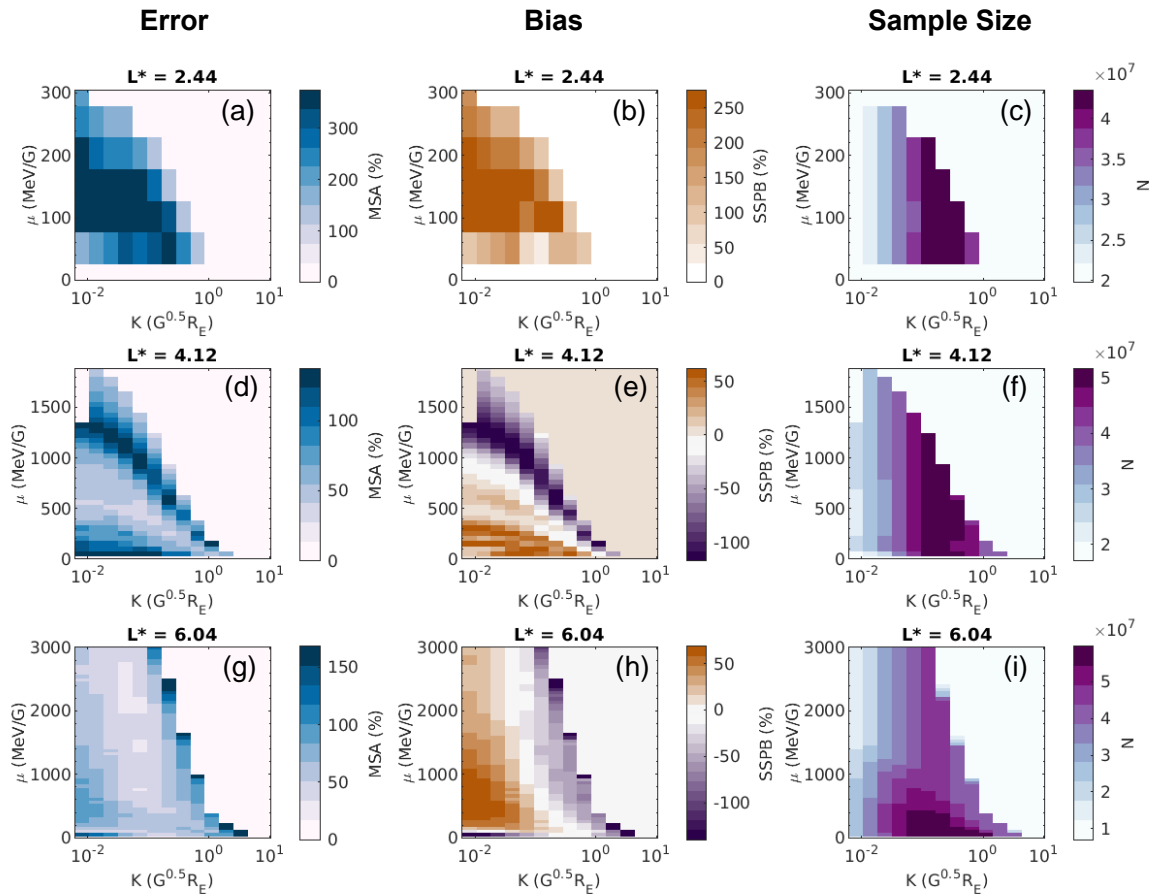
208 All spacecraft data is calibrated to Van Allen Probe B and bias-corrected GOES 15 data, which  
209 are chosen as the "gold standards" for the calibration. The GPS pitch angle distributions are  
210 assumed using the Zhao et al. (2018) model. For each spacecraft instrument, the adiabatic  
211 invariants  $\mu$ ,  $K$ , and  $L^*$  are computed using a model magnetospheric field, represented by the  
212 International Geomagnetic Reference Field model (IGRF; Thébault et al., 2015) and Tsyganenko  
213 (1989) external magnetic field model (T89). The final PSD dataset is interpolated across  
214 dimensions of  $\mu$  and  $K$ , but not across  $L^*$  or time.

## 215 4 Validation Results

### 216 4.1 Original Forecast Framework (2016-2018)

217 Figure 3 shows the MSA, SSPB, and number of samples,  $N$ , calculated for the 10-hour hindcast of  
218 radiation belt PSD as a function of the first and second adiabatic invariants,  $\mu$  and  $K$  at three  
219 sampled  $L^*$ . The  $L^*$  values shown in Figure 3 are selected to represent trends in error and bias

220 observed in the slot region ( $\sim L^* = 2.44$ ), the core of the outer radiation belt, and the outer  
 221 radiation belt near medium earth orbit ( $\sim L^* = 4.12$ ) and at geostationary orbit ( $\sim L^* = 6.04$ ).



222

223 **Figure 3** Left column shows the statistical error (MSA) of the 10-hour hindcast between  
 224 **2016-2018**, shown by color as a function of  $\mu$  and  $K$  for a sample of simulated  $L^* = 2.44$ ,  
 225 **4.12**, and **6.04**. The middle column shows statistical bias (SSPB) in the same format, and  
 226 **right** column shows the number of samples  $N$  used in the computation of MSA and SSPB.

227 We observe a large variance in the MSA and SSPB across the different  $L^*$  regions. At  $L^* = 2.44$  the  
 228 maximum percentage error was 350%, and the maximum bias was 250%. At  $L^* = 2.44$ , electrons  
 229 are generally located inside the overlapping plasmasphere and slot region, so the large positive  
 230 bias indicates that the model systematically overestimated the PSD in the slot region. It is because  
 231 electron PSD is generally very low at  $L^* < 4$ , that comparatively small absolute differences in PSD  
 232 create large errors and bias relative to the measured PSD.

233 In the outer radiation belt region ( $L^* > 4$ ) the error and bias were much smaller than the slot  
234 region, reaching a maximum of 150% percentage error and -150% bias. This indicates that  
235 statistically the hindcast accurately predicted the outer radiation belt PSD to within a factor of 1.5.  
236 Moreover, the hindcast error and bias was highly dependent upon  $\mu$  and  $K$ .

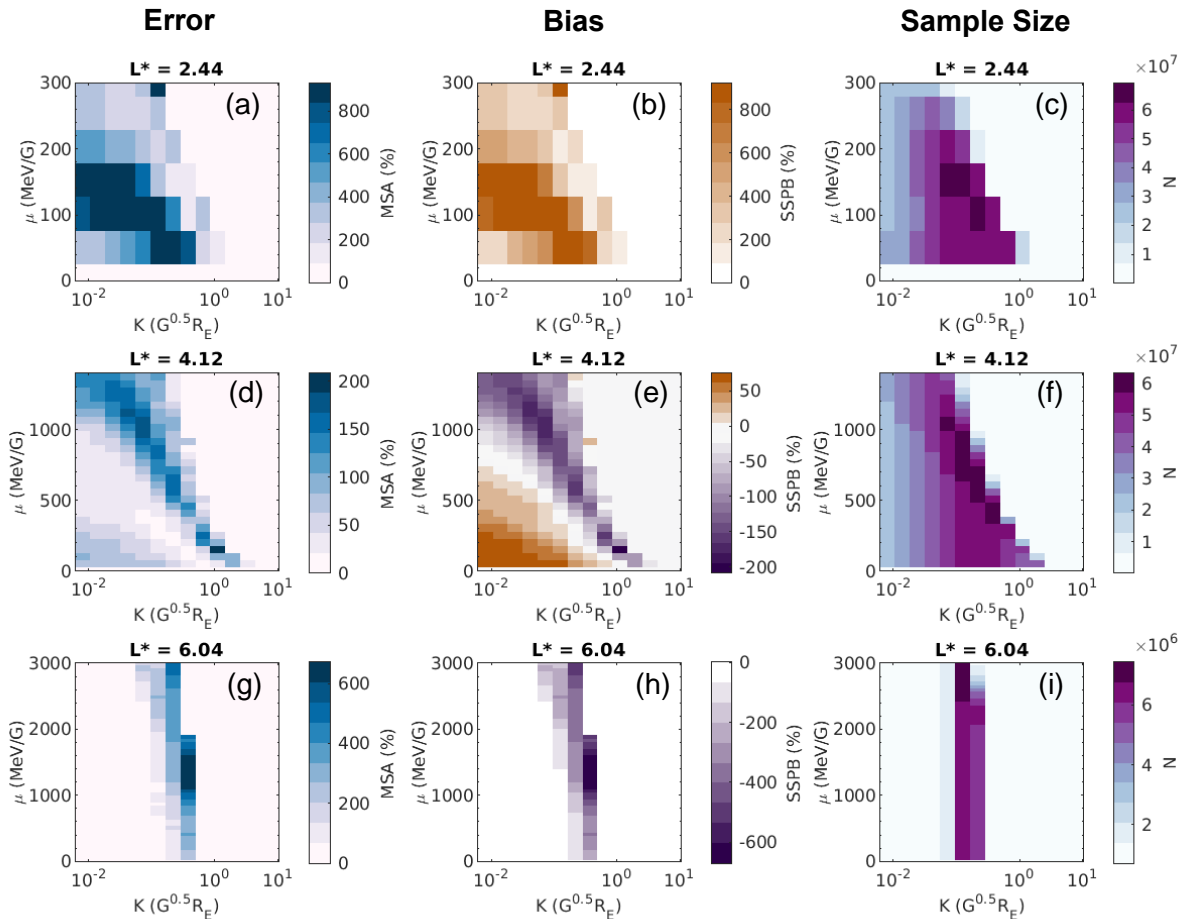
237 At  $L^* = 4.12$  the greatest errors were found to reach 150% corresponding to the highest  
238 measured  $\mu$  values depending on  $K$  (i.e., highest energies,  $\sim$  multi-MeV) and was  
239 correspondingly biased toward underestimation of PSD by  $\sim$ 120%. At lower  $\mu$  values (which  
240 correspond to the bulk of the radiation belt plasma population) the hindcast showed a statistical  
241 overestimation of PSD by 70% or less, showing that the hindcast predicted the core outer belt  
242 PSD to within a factor of 0.7. The hindcast error and bias showed similar trends at  $L^* = 6.04$ : The  
243 highest errors were observed at the highest measured  $\mu$  (highest energies) with a negative bias  
244  $> -100\%$ , and at lower  $\mu$  the hindcast overestimated PSD by up to 70%. In addition to these  
245 error and bias relationships, at  $L^* = 6.04$  there was a strong error of 150% and bias of -150%  
246 observed at  $\mu < 100$  MeV/G. This population corresponds to lower energy  $< 300$  keV electron  
247 populations. To ensure that error and bias is not dependent upon hindcast hour, the same  
248 analysis was completed for different hindcast hour, and no appreciable differences were  
249 observed.

250 The following analysis discusses the source of the statistical hindcast error and bias and  
251 evaluates the accuracy of the hindcast under different geomagnetic conditions.

#### 252 4.1.1 Assimilated Data Bias

253 One potential source of error in the model hindcast is assimilated data bias. Between 2016-2018  
254 the assimilated datasets were real time GOES data, and the Van Allen Probe Beacon data.  
255 Because the assimilated GOES data is similar to the final science data product, it is not  
256 informative to evaluate the bias of this data. The Van Allen Probe beacon data was provided in  
257 real time over the Van Allen Probe mission without the same corrections and post-processing as  
258 the long-term science data archive, and so is possibly more prone to errors. To assess if the  
259 error and bias of assimilated PSD observations influenced the hindcast PSD, we will evaluate the  
260 error and bias of the Van Allen Probe Beacon data (Figure 4) and compare the hindcast error

261 and bias (Figure 3). The error and bias of Van Allen Probe beacon data is quantified by  
 262 calculating the MSA and SSPB respectively using Equation 2 and Equation 3, where the quotient  
 263 is calculated as  $Q = PSD_{Beacon}/PSD_{Final}$ , and  $PSD_{Final}$  is the science data product from the  
 264 same Van Allen Probe. This analysis effectively shows the differences between the real time data  
 265 product and the more highly processed science data as a function of  $\mu$ ,  $K$ , and  $L^*$ .



266

267 **Figure 4 Left column shows the statistical error (MSA) and middle column shows the**  
 268 **statistical bias (SSPB) of the Van Allen Probe B beacon data between 2016-2018,**  
 269 **compared to the final Van Allen Probe science data. Right column shows the number of**  
 270 **data samples  $N$  used in the computation of MSA and SSPB. Error, bias, and sample size are**  
 271 **all shown by color as a function of  $\mu$  and  $K$  at sampled bins of  $L^* = 2.44; 4.12; 6.04$  which**  
 272 **were chosen to match the hindcast model grid.**

273 Figure 4 shows that universally (i.e., all  $L^*$ ,  $\mu$ , and  $K$ ), the error and bias for Van Allen Probe  
 274 beacon data was greater than the hindcast error and bias (Figure 3). For example, at  $L^* = 2.44$ ,

275 both the error and bias of beacon data reached  $> 800\%$ , whereas the maximum hindcast error  
276 and bias were  $\sim 350\%$  and  $\sim 250\%$  respectively. The magnitude difference in error and bias was  
277 less significant at  $L^* = 4.12$ , which reached a maximum of  $200\%$  error and  $-200\%$  respectively.

278 Despite differences in magnitude, we highlight that the error and bias observed for Van Allen  
279 Probe beacon data (Figure 4) was nearly identically distributed across  $\mu$ ,  $K$ , and  $L^*$  compared to  
280 the 10-hour hindcast error and bias. For example, at  $L^* = 4.12$ , the maximum errors were at the  
281 highest  $\mu$  values across all  $K$ , and were negatively biased, transitioning to a positive bias at low  $\mu$   
282 values. This observation shows that the assimilated data significantly influenced the error and  
283 bias of the hindcast. Though, because the magnitude of the hindcast error and bias was less  
284 than the assimilated data, the simulated hindcast gave a significantly improved estimation of  
285 radiation belt PSD than if Van Allen Probe beacon data was used alone.

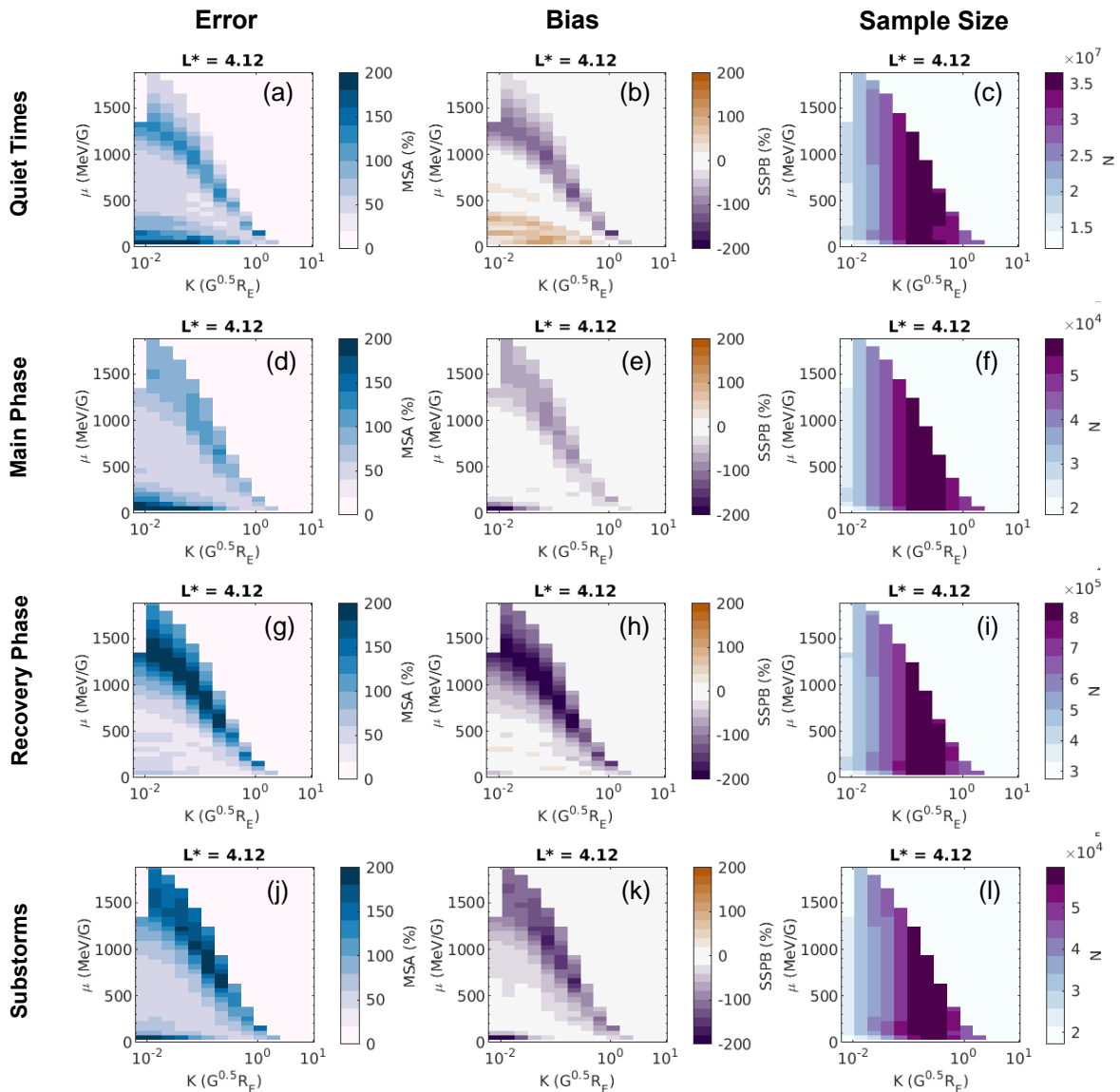
#### 286 4.1.2 Storm-time Error Analysis

287 Knowing how well the model captures the radiation belt evolution during different geomagnetic  
288 conditions is of particular interest because most impacts to satellites are observed during  
289 geomagnetically active periods. To analyze how the statistical error and bias varies with  
290 geomagnetic conditions, we extract geomagnetic storm intervals between 2016-2018 based  
291 upon Sym-H index evolution. A storm is identified by time periods where Sym-H decreased  
292 below  $-40$  nT. The main storm phase is classified from intervals when Sym-H decreased from a  
293 value above  $15$  nT, to a Sym-H minimum below  $-40$  nT. The recovery storm phase is classified  
294 from when the Sym-H increased after the main storm phase, until it reached a value above  $-15$   
295 nT. We further select times during geomagnetic storms when the AE index was in the upper 80%  
296 percentile of data. High AE index periods are known to be associated with substorm injections of  
297 lower energy source electrons from the magnetotail into the inner magnetosphere, and AE index  
298 values exceeding  $150$  nT have previously been used as a proxy for substorm injections (e.g.,  
299 Meredith et al., 2000). As before, we calculate the statistical error and bias of each storm phase  
300 using Equation 2 and Equation 3. Figure 5 and Figure 6 show how the computed error and bias  
301 varied under different geomagnetic conditions at  $L^* = 4.12$  and  $L^* = 6.04$ , respectively. To easily  
302 compare between geomagnetic conditions, the color bars have been saturated to  $\pm 200\%$ . We

303 do not show the equivalent figure for  $L^* = 2.44$  as no substantial differences between storm  
304 phases were observed.

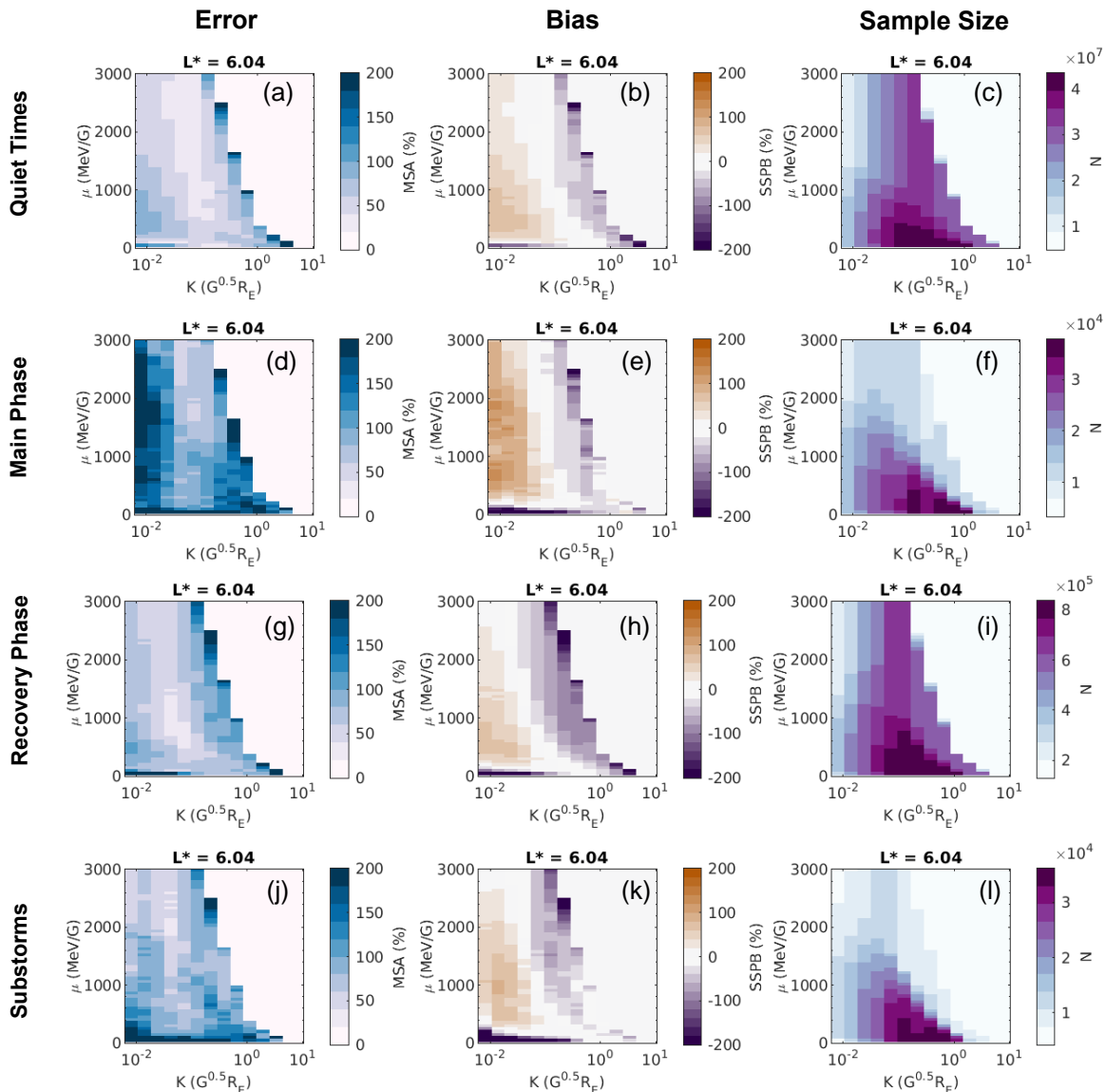
305 Firstly, we observe from Figure 5 that the statistical error and bias under geomagnetically quiet  
306 conditions were effectively the same as for all data between 2016-2019 shown in Figure 3. This  
307 indicates that the overall statistical error and bias for the hindcast at  $L^* = 4.12$  was not  
308 influenced by increased error or bias during geomagnetic variations. Figure 5 g-h show that high  
309  $\mu$  values (highest energies  $\geq$  MeV) appear least accurate and most biased during the recovery  
310 storm phase (and during substorm injections) as MSA increased to 200% at the highest  $\mu$  values  
311 (panel g), and SSPB decreases to -200% (panel h). This indicates that, during the recovery phase,  
312 the hindcast underestimated the PSD of MeV electrons, which is understood to become  
313 enhanced during this phase (e.g., Jaynes et al., 2015; K. R. Murphy et al., 2018; Sorathia et al.,  
314 2018). Conversely, PSD of low  $\mu$  electrons ( $\approx 700$  keV for) is less accurate during the main storm  
315 phase (panel d), and during substorm related injections (panel j-k). In both cases the error is  
316 observed to reach 200% and the hindcast was biased towards underestimation of PSD down to -  
317 200%. Figure 5 shows that the hindcast consistently underestimated PSD across all storm  
318 conditions at  $L^* = 4.12$ , for all  $\mu$  and  $K$ .

319 Similarly, Figure 6 shows that at  $L^* = 6.04$ , quiet times exhibited the same statistical error and  
320 bias as the overall time period (Figure 3), and PSD of high  $\mu$  (energies  $\geq$  MeV) were the least  
321 accurate and most biased during the recovery phase of the storm (Figure 6 g-h). However,  
322 Figure 6d shows that, irrespective of  $\mu$ , the largest overall errors were observed at low  $K$  (i.e.,  
323 equatorial electrons) during the main storm phase. Given Figure 6e shows a bias towards  
324 overestimation of PSD at these  $K$ , and that  $L^* = 6.04$  is near geostationary orbit, it is possible  
325 that loss to the outer boundary was not well captured by the hindcast. Figure 6j also shows large  
326 hindcast errors for  $\mu < 500$  MeV/G, and bias towards underestimation of PSD by up to -200%.  
327 Since this feature was most prominent during storms with the highest AE index, we expect these  
328 errors were caused by substorm injections of lower-energy (<500 keV) electrons.



329

330 **Figure 5** Left column shows the statistical error (MSA) and middle column shows the  
 331 **statistical bias (SSPB) of the 10-hour hindcast between 2016-2018, compared to the final**  
 332 **multi-mission PSD observations. Right column shows the number of data samples N used**  
 333 **in the computation of MSA and SSPB. Error, bias, and sample size are all shown by color**  
 334 **as a function of  $\mu$  and  $K$  at sampled bins of  $L^* = 4.12$ . Each row shows error and bias under**  
 335 **different geomagnetic conditions a-c are quiet times, d-f are the main storm phase, g-l**  
 336 **are the recovery storm phase, and j-l show storm intervals which contain substorm**  
 337 **injections.**



338

339 **Figure 6 Statistical error and bias under different geomagnetic conditions, sampled at  $L^* =$**   
 340 **6.04 is shown in the same format as Figure 5.**

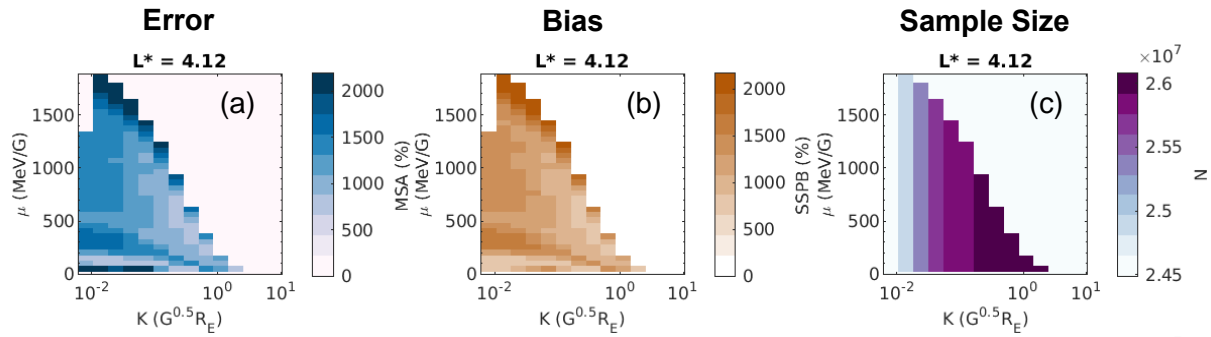
341 **4.2 Updated Forecast Framework (2019-2020)**

342 Since the end of the Van Allen Probe mission in early 2019, the RBFMF has been operating by  
 343 assimilating only GOES observations in real time. To assess how this affected the accuracy of the  
 344 10 hour hindcast, we repeat the analysis presented in the previous section, comparing the 10  
 345 hour hindcast at  $L^* = 4.2$  to PSD observations obtained from the GPS constellation between  
 346 March 2019 – December 2020 (Figure 7). Since the real-time GOES data assimilated into the

347 hindcast model is similar to the final science data product, it is not meaningful to complete an  
348 error analysis at geostationary orbit using this data.

349 Figure 7 shows that the hindcast error and bias at  $L^* = 4.12$  were significantly increased  
350 compared to the Van Allen Probe era (Figure 3), reaching maxima of  $> 2000\%$ , which is a factor  
351 of 10 greater than was observed between 2016-2018. The hindcast was strongly biased towards  
352 overestimation of PSD at all  $\mu$  and  $K$  values by similar magnitudes to the error, which suggests  
353 that the model could be improved by the inclusion of a corrective factor. It is important to note  
354 that GPS satellites do not resolve electron flux by pitch angle, so an assumed pitch angle  
355 distribution is used to calculate PSD as a function of  $\mu$ ,  $K$ , and  $L^*$ . It is possible that error and bias  
356 determined at  $L^* = 4.12$  were affected by the assumed pitch angle distribution used in GPS data  
357 processing, rather than actual errors in the hindcast. Another dataset of PSD observations which  
358 are pitch angle resolved is needed to test if this is the case (e.g., ARASE).

359 We emphasize that the diffusive simulation driving the hindcast provided a good first  
360 approximation of radiation belt dynamics, but is somewhat rudimentary as simplified diffusive  
361 modelling was employed. However, we chose not to modify the forecast model until a  
362 comprehensive analysis of hindcast performance was conducted. Since less observational data is  
363 now available to constrain the hindcast via data assimilation, the diffusion simulation should be  
364 improved by updating the precomputed diffusion coefficients using more modern  
365 methodologies of representing Chorus (e.g., Wong et al., 2024), Hiss (e.g., Agapitov et al., 2020;  
366 Watt et al., 2019 ), and ULF waves (e.g., Kyle R. Murphy et al., 2023). The diffusive effects of EMIC  
367 waves could also be incorporated (e.g., Ross et al., 2020) to improve the representation of  
368 electron loss in the inner magnetosphere.



369

370 **Figure 7** Statistical error (MSA, panel a) and bias (SSPB, panel b) are of the 10-hour  
 371 hindcast in 2019-2020 are shown as a function of  $\mu$  and  $K$  at  $L^* = 4.12$ . The number of data  
 372 samples,  $N$ , is shown in the panel c.

## 373 5 Summary

374 We have conducted a comprehensive assessment of the accuracy and bias of the Radiation Belt  
 375 Forecasting Model and Framework, which is used to specify the real-time radiation environment  
 376 in the Satellite Charging Assessment Tool. Historical hindcasts were compared to observations  
 377 of the radiation belt by computing the statistical errors and bias between the years January 2016  
 378 – October 2018 while the Van Allen Probes remained in operation, and between March 2019 –  
 379 December 2020 following the end of the Van Allen Probe mission.

380 The hindcast was found to be accurate to within a factor of 1.5 in the outer radiation belt ( $4 < L^*$   
 381  $< 7$ ) during the years when the Van Allen Probe data was assimilated into the model (Figure  
 382 3d,g). We identified that the statistical hindcast bias was predominantly introduced by the  
 383 assimilated Van Allen Probe data, which displayed the same dependence of bias upon  $\mu$  and  $K$   
 384 (Figure 4). Analysis of geomagnetic storms between 2016-2018 also revealed increased hindcast  
 385 error and bias compared to quiet times at  $L^* > 4$ . The most energetic electrons ( $> \text{MeV}$ ) were  
 386 more likely to be underestimated by the hindcast during storm recovery phase (Figure 5), error  
 387 increased for equatorial electrons at  $L^* \sim 6$  during the main storm phase (Figure 6d), and the  
 388 hindcast underestimated lower energy electrons ( $< 500 \text{ keV}$ ) related to substorm injections  
 389 (Figure 6j).

390 We have shown that the hindcast was much more accurate at predicting PSD than if the Van  
391 Allen Probe beacon data was used alone (Figure 4). Moreover, we found that the Van Allen  
392 Probe beacon data played a crucial role in constraining hindcast simulation between 2016-2019  
393 as the hindcast error and bias increased tenfold when the Van Allen Probe data was no longer  
394 available (2018-2020). This highlights that combining coarsely processed data with physics-  
395 based modelling through data assimilation can improve the accuracy of radiation environment  
396 specification than either method used alone.

## 397 6 Future Work

398 Our analysis has emphasized the importance of real-time observations at multiple locations  
399 through the outer radiation belt. Even though the beacon Van Allen Probe data contained  
400 significant error and bias compared to the final processed data, assimilation of these  
401 observations into the RBFMF considerably improved the simulation compared to times where it  
402 was not assimilated. Furthermore, we showed that data assimilative techniques displayed  
403 reduced error and bias compared to the real time observations which were coarsely processed  
404 compared to final processed science data. Since the end of the Van Allen Probe mission, there  
405 are no similar observations available as the currently operational observatories (e.g., GPS,  
406 ARASE) do not provide publicly available data in real time. We emphasize that any provision of  
407 real time observations from existing or new missions enhance the operational impact of data,  
408 even if it is sub-optimally processed compared to science quality data. Furthermore, analysis of  
409 real-time data errors, analogous to our analysis of beacon Van Allen Probe data, can be used to  
410 inform the observational uncertainties used during data assimilation simulations.

411 In lieu of real-time observations to constrain this stimulation through the heart of the radiation  
412 belt, our analysis has highlighted key areas in which the physics simulation could be improved.  
413 Overestimation of PSD in the plasmasphere could be addressed by evaluating more recent  
414 diffusion coefficients computed for Plasmaspheric Hiss (e.g., Agapitov et al., 2020; Watt et al.,  
415 2019). Improved representation of electron loss at geostationary orbit during the storm main  
416 phase could be incorporated by using a dynamic outer boundary of the simulation (Bloch et al.,  
417 2021; Staples et al., 2020) and evaluating new radial diffusion coefficients (Kyle R. Murphy et al.,

418 2023). Updating the radial diffusion coefficients could also improve hindcast with sparse real-  
419 time data by accurately propagating the effects of assimilated data across  $L^*$ . Underestimation  
420 of ultra-relativistic electrons during the storm recovery phase could be improved by updating  
421 energy diffusion through new parameterizations of Chorus waves (e.g., Wong et al., 2024).  
422 Furthermore, substorm injections of lower energy electrons are necessary, and could be  
423 incorporated through updates to the simulation boundaries. Continued development of the  
424 physics-based simulation is ongoing so that new versions of the RBFMF can be provided with  
425 improved hindcast accuracy.

## Acknowledgements

FS and ACK acknowledge support from NASA grants 80NSSC20K1402 and 80NSSC23K0096 and NSF grant 2149782, and JG acknowledges acknowledge support from NASA grant 80NSSC20K1402 and NSF grant 2149782.

## Open Research

Spacecraft data from GOES and the Van Allen Probes are publicly available via the NASA/GSFC CDAWeb service (<https://cdaweb.gsfc.nasa.gov/index.html/>). Solar Wind data and geomagnetic indices are publicly available through the NASA/GSFC Space Physics Data Facility OMNIWeb service (<https://omniweb.gsfc.nasa.gov/>). Due to the size of the specification model output and the electron PSD reference dataset, these cannot be hosted on an online repository platform, but will be made available upon request.

## References

- Agapitov, O., Mourenas, D., Artemyev, A., Claudepierre, S. G., Hospodarsky, G., & Bonnell, J. W. (2020). Lifetimes of Relativistic Electrons as Determined From Plasmaspheric Hiss Scattering Rates Statistics: Effects of  $\omega_{pe}/\Omega_{ce}$  and Wave Frequency Dependence on Geomagnetic Activity. *Geophysical Research Letters*, 47(13), e2020GL088052. <https://agupubs.onlinelibrary.wiley.com/doi/abs/10.1029/2020GL088052>
- Angelopoulos, V. (2008). The THEMIS Mission. *Space Science Reviews*, 141(1), 5. <https://doi.org/10.1007/s11214-008-9336-1>
- Angelopoulos, V., Sibeck, D., Carlson, C. W., McFadden, J. P., Larson, D., Lin, R. P., et al. (2008). First Results from the THEMIS Mission. *Space Science Reviews*, 141(1), 453-476. <https://doi.org/10.1007/s11214-008-9378-4>
- Baker, D. N., Kanekal, S. G., Hoxie, V. C., Batiste, S., Bolton, M., Li, X., et al. (2014). The Relativistic Electron-Proton Telescope (REPT) Instrument on Board the Radiation Belt Storm Probes (RBSP) Spacecraft: Characterization of Earth's Radiation Belt High-Energy Particle Populations. In N. Fox & J. L. Burch (Eds.), *The Van Allen Probes Mission* (pp. 337-381). Boston, MA: Springer US.
- Blake, J. B., Carranza, P. A., Claudepierre, S. G., Clemmons, J. H., Crain, W. R., Dotan, Y., et al. (2014). The Magnetic Electron Ion Spectrometer (MagEIS) Instruments Aboard the Radiation Belt Storm Probes (RBSP) Spacecraft. In N. Fox & J. L. Burch (Eds.), *The Van Allen Probes Mission* (pp. 383-421). Boston, MA: Springer US.
- Blake, J. B., Mauk, B. H., Baker, D. N., Carranza, P., Clemmons, J. H., Craft, J., et al. (2016). The Fly's Eye Energetic Particle Spectrometer (FEEPS) Sensors for the Magnetospheric Multiscale (MMS) Mission. *Space Science Reviews*, 199, 309. <https://ui.adsabs.harvard.edu/abs/2016SSRv..199..309B>
- Bloch, T., Watt, C. E. J., Owens, M. J., Thompson, R. L., & Agiwal, O. (2021). Constraining the Location of the Outer Boundary of Earth's Outer Radiation Belt. *Earth and Space Science*, 8(6), e2020EA001610. <https://agupubs.onlinelibrary.wiley.com/doi/abs/10.1029/2020EA001610>
- Boyd, A. J., Green, J. C., O'Brien, T. P., & Claudepierre, S. G. (2023). Specifying High Altitude Electrons Using Low-Altitude LEO Systems: Updates to the SHELLS Model. *Space Weather*, 21(3), e2022SW003338. <https://agupubs.onlinelibrary.wiley.com/doi/abs/10.1029/2022SW003338>
- Brautigam, D. H., & Albert, J. M. (2000). Radial diffusion analysis of outer radiation belt electrons during the October 9, 1990, magnetic storm. *Journal of Geophysical Research: Space Physics*, 105(A1), 291-309. <https://agupubs.onlinelibrary.wiley.com/doi/abs/10.1029/1999JA900344>
- Burch, J. L., Moore, T. E., Torbert, R. B., & Giles, B. L. (2016). Magnetospheric Multiscale Overview and Science Objectives. *Space Science Reviews*, 199(1), 5-21. <https://doi.org/10.1007/s11214-015-0164-9>

- Camporeale, E. (2019). The Challenge of Machine Learning in Space Weather: Nowcasting and Forecasting. *Space Weather*, 17(8), 1166-1207.  
<https://agupubs.onlinelibrary.wiley.com/doi/abs/10.1029/2018SW002061>
- Chen, Y., Reeves, G. D., Fu, X., & Henderson, M. (2019). PreMevE: New Predictive Model for Megaelectron-Volt Electrons Inside Earth's Outer Radiation Belt. *Space Weather*, 17(3), 438-454. <https://agupubs.onlinelibrary.wiley.com/doi/abs/10.1029/2018SW002095>
- Coleman, T., McCollough, J. P., Young, S., & Rigler, E. J. (2018). Operational Nowcasting of Electron Flux Levels in the Outer Zone of Earth's Radiation Belt. *Space Weather*, 16(5), 501-518. <https://agupubs.onlinelibrary.wiley.com/doi/abs/10.1029/2017SW001788>
- Daae, M., Shprits, Y. Y., Ni, B., Koller, J., Kondrashov, D., & Chen, Y. (2011). Reanalysis of radiation belt electron phase space density using various boundary conditions and loss models. *Advances in Space Research*, 48(8), 1327-1334.  
<https://www.sciencedirect.com/science/article/pii/S0273117711004741>
- Fennell, J. F., Koons, H. C., Roeder, J. L., & Blake, J. B. (2001). Spacecraft charging: Observations and relationship to satellite anomalies. *Spacecraft Charging Technology, Proceedings of the Seventh International Conference, European Space Agency Special Publication, ESA SP-476*, 279-284.
- Galvan, D. A., Hemenway, B., Welsler, W., & Baiocchi, D. (2014). *Satellite Anomalies Benefits of a Centralized Anomaly Database and Methods for Securely Sharing Information Among Satellite Operators*: RAND Corporation.
- Green, J. C., Likar, J., & Shprits, Y. (2017). Impact of space weather on the satellite industry. *Space Weather*, 15(6), 804-818.  
<https://agupubs.onlinelibrary.wiley.com/doi/abs/10.1002/2017SW001646>
- Horne, R. B., Glauert, S. A., Meredith, N. P., Boscher, D., Maget, V., Heynderickx, D., & Pitchford, D. (2013). Space weather impacts on satellites and forecasting the Earth's electron radiation belts with SPACECAST. *Space Weather*, 11(4), 169-186.  
<https://agupubs.onlinelibrary.wiley.com/doi/abs/10.1002/swe.20023>
- Jaynes, A. N., Baker, D. N., Singer, H. J., Rodriguez, J. V., Loto'aniu, T. M., Ali, A. F., et al. (2015). Source and seed populations for relativistic electrons: Their roles in radiation belt changes. *Journal of Geophysical Research: Space Physics*, 120(9), 7240-7254.  
<https://agupubs.onlinelibrary.wiley.com/doi/abs/10.1002/2015JA021234>
- Kalman, R. E. (1960). A New Approach to Linear Filtering and Prediction Problems. *Journal of Basic Engineering*, 82(1), 35-45. <https://doi.org/10.1115/1.3662552>
- Kellerman, A. C. (2018). Chapter 10 - Prediction of MeV Electron Fluxes and Forecast Verification. In E. Camporeale, S. Wing, & J. R. Johnson (Eds.), *Machine Learning Techniques for Space Weather* (pp. 259-278): Elsevier.
- Kellerman, A. C., Shprits, Y. Y., Kondrashov, D., Subbotin, D., Makarevich, R. A., Donovan, E., & Nagai, T. (2014). Three-dimensional data assimilation and reanalysis of radiation belt

- electrons: Observations of a four-zone structure using five spacecraft and the VERB code. *Journal of Geophysical Research: Space Physics*, 119(11), 8764-8783.  
<https://agupubs.onlinelibrary.wiley.com/doi/abs/10.1002/2014JA020171>
- Kondrashov, D., Shprits, Y., Ghil, M., & Thorne, R. (2007). A Kalman filter technique to estimate relativistic electron lifetimes in the outer radiation belt. *Journal of Geophysical Research: Space Physics*, 112(A10).  
<https://agupubs.onlinelibrary.wiley.com/doi/abs/10.1029/2007JA012583>
- Koons, H., Mazur, J., Selesnick, R., Blake, J., Fennell, J., Roeder, J., & Anderson, P. (1999). The impact of the space environment on space systems. *NASA STI/Recon Technical Report N*, 69036-69041.
- Li, W., Shprits, Y. Y., & Thorne, R. M. (2007). Dynamic evolution of energetic outer zone electrons due to wave-particle interactions during storms. *Journal of Geophysical Research: Space Physics*, 112(A10).  
<https://agupubs.onlinelibrary.wiley.com/doi/abs/10.1029/2007JA012368>
- Li, X. (2004). Variations of 0.7–6.0 MeV electrons at geosynchronous orbit as a function of solar wind. *Space Weather*, 2(3).  
<https://agupubs.onlinelibrary.wiley.com/doi/abs/10.1029/2003SW000017>
- Lohmeyer, W., Carlton, A., Wong, F., Bodeau, M., Kennedy, A., & Cahoy, K. (2015). Response of geostationary communications satellite solid-state power amplifiers to high-energy electron fluence. *Space Weather*, 13(5), 298-315.  
<https://agupubs.onlinelibrary.wiley.com/doi/abs/10.1002/2014SW001147>
- McFadden, J. P., Carlson, C. W., Larson, D., Ludlam, M., Abiad, R., Elliott, B., et al. (2008). The THEMIS ESA Plasma Instrument and In-flight Calibration. *Space Science Reviews*, 141(1), 277-302. <https://doi.org/10.1007/s11214-008-9440-2>
- Meredith, N. P., Horne, R. B., Johnstone, A. D., & Anderson, R. R. (2000). The temporal evolution of electron distributions and associated wave activity following substorm injections in the inner magnetosphere. *Journal of Geophysical Research: Space Physics*, 105(A6), 12907-12917. <https://agupubs.onlinelibrary.wiley.com/doi/abs/10.1029/2000JA900010>
- Morley, S. K., Brito, T. V., & Welling, D. T. (2018). Measures of Model Performance Based On the Log Accuracy Ratio. *Space Weather*, 16(1), 69-88.  
<https://agupubs.onlinelibrary.wiley.com/doi/abs/10.1002/2017SW001669>
- Morley, S. K., Sullivan, J. P., Carver, M. R., Kippen, R. M., Friedel, R. H. W., Reeves, G. D., & Henderson, M. G. (2017). Energetic Particle Data From the Global Positioning System Constellation. *Space Weather*, 15(2), 283-289.  
<https://agupubs.onlinelibrary.wiley.com/doi/abs/10.1002/2017SW001604>
- Murphy, K. R., Sandhu, J., Rae, I. J., Daggitt, T., Glauert, S., Horne, R. B., et al. (2023). A New Four-Component L\*-Dependent Model for Radial Diffusion Based on Solar Wind and Magnetospheric Drivers of ULF Waves. *Space Weather*, 21(7), e2023SW003440.  
<https://agupubs.onlinelibrary.wiley.com/doi/abs/10.1029/2023SW003440>

- Murphy, K. R., Watt, C. E. J., Mann, I. R., Jonathan Rae, I., Sibeck, D. G., Boyd, A. J., et al. (2018). The Global Statistical Response of the Outer Radiation Belt During Geomagnetic Storms. *Geophysical Research Letters*, 45(9), 3783-3792.  
<https://agupubs.onlinelibrary.wiley.com/doi/abs/10.1002/2017GL076674>
- Naehr, S. M., & Toffoletto, F. R. (2005). Radiation belt data assimilation with an extended Kalman filter. *Space Weather*, 3(6).  
<https://agupubs.onlinelibrary.wiley.com/doi/abs/10.1029/2004SW000121>
- Nagai, T. (1988). "Space weather forecast": Prediction of relativistic electron intensity at synchronous orbit. *Geophysical Research Letters*, 15(5), 425-428.  
<https://agupubs.onlinelibrary.wiley.com/doi/abs/10.1029/GL015i005p00425>
- Ni, B., Shprits, Y., Nagai, T., Thorne, R., Chen, Y., Kondrashov, D., & Kim, H.-j. (2009). Reanalyses of the radiation belt electron phase space density using nearly equatorial CRRES and polar-orbiting Akebono satellite observations. *Journal of Geophysical Research: Space Physics*, 114(A5). <https://agupubs.onlinelibrary.wiley.com/doi/abs/10.1029/2008JA013933>
- Rodriguez, J. V. (2014a). *GOES 13-15 MAGE/PD pitch angles algorithm theoretical basis document*. Retrieved from  
<https://ngdc.noaa.gov/stp/satellite/goes/documentation.html>.
- Rodriguez, J. V. (2014b). *GOES EPEAD science-quality electron fluxes algorithm theoretical basis document*. Retrieved from  
[https://ngdc.noaa.gov/stp/satellite/goes/doc/EPEAD\\_Electron\\_Science\\_Reprocessing\\_ATB\\_D\\_v1.0.pdf](https://ngdc.noaa.gov/stp/satellite/goes/doc/EPEAD_Electron_Science_Reprocessing_ATB_D_v1.0.pdf)
- Roeder, J. L., Chen, M. W., Fennell, J. F., & Friedel, R. (2005). Empirical models of the low-energy plasma in the inner magnetosphere. *Space Weather*, 3(12).  
<https://agupubs.onlinelibrary.wiley.com/doi/abs/10.1029/2005SW000161>
- Roederer, J. (1970). Dynamics of Geomagnetically Trapped Radiation, Phys. and Chem. *Space*, 2, 166.
- Ross, J. P. J., Glauert, S. A., Horne, R. B., Watt, C. E., Meredith, N. P., & Woodfield, E. E. (2020). A New Approach to Constructing Models of Electron Diffusion by EMIC Waves in the Radiation Belts. *Geophysical Research Letters*, 47(20), e2020GL088976.  
<https://agupubs.onlinelibrary.wiley.com/doi/abs/10.1029/2020GL088976>
- Schulz, M., & Lanzerotti, L. J. (1974). Particle diffusion in the radiation belts. *Physics and Chemistry in Space*.
- Sheeley, B. W., Moldwin, M. B., Rassoul, H. K., & Anderson, R. R. (2001). An empirical plasmasphere and trough density model: CRRES observations. *Journal of Geophysical Research: Space Physics*, 106(A11), 25631-25641.  
<https://agupubs.onlinelibrary.wiley.com/doi/abs/10.1029/2000JA000286>
- Shin, D.-K., Lee, D.-Y., Kim, K.-C., Hwang, J., & Kim, J. (2016). Artificial neural network prediction model for geosynchronous electron fluxes: Dependence on satellite position and particle

- energy. *Space Weather*, 14(4), 313-321.  
<https://agupubs.onlinelibrary.wiley.com/doi/abs/10.1002/2015SW001359>
- Shprits, Y., Kellerman, A., Kondrashov, D., & Subbotin, D. (2013). Application of a new data operator-splitting data assimilation technique to the 3-D VERB diffusion code and CRRES measurements. *Geophysical Research Letters*, 40(19), 4998-5002.  
<https://agupubs.onlinelibrary.wiley.com/doi/abs/10.1002/grl.50969>
- Shprits, Y., Kondrashov, D., Chen, Y., Thorne, R., Ghil, M., Friedel, R., & Reeves, G. (2007). Reanalysis of relativistic radiation belt electron fluxes using CRRES satellite data, a radial diffusion model, and a Kalman filter. *Journal of Geophysical Research: Space Physics*, 112(A12). <https://agupubs.onlinelibrary.wiley.com/doi/abs/10.1029/2007JA012579>
- Sillanpää, I., Ganushkina, N. Y., Dubyagin, S., & Rodriguez, J. V. (2017). Electron Fluxes at Geostationary Orbit From GOES MAGED Data. *Space Weather*, 15(12), 1602-1614.  
<https://agupubs.onlinelibrary.wiley.com/doi/abs/10.1002/2017SW001698>
- Sorathia, K. A., Ukhorskiy, A. Y., Merkin, V. G., Fennell, J. F., & Claudepierre, S. G. (2018). Modeling the Depletion and Recovery of the Outer Radiation Belt During a Geomagnetic Storm: Combined MHD and Test Particle Simulations. *Journal of Geophysical Research: Space Physics*, 123(7), 5590-5609.  
<https://agupubs.onlinelibrary.wiley.com/doi/abs/10.1029/2018JA025506>
- Spasojevic, M., Shprits, Y. Y., & Orlova, K. (2015). Global empirical models of plasmaspheric hiss using Van Allen Probes. *Journal of Geophysical Research: Space Physics*, 120(12), 10,370-310,383. <https://agupubs.onlinelibrary.wiley.com/doi/abs/10.1002/2015JA021803>
- Staples, F. A., Kellerman, A., Murphy, K. R., Rae, I. J., Sandhu, J. K., & Forsyth, C. (2022). Resolving Magnetopause Shadowing Using Multimission Measurements of Phase Space Density. *Journal of Geophysical Research: Space Physics*, 127(2), e2021JA029298.  
<https://agupubs.onlinelibrary.wiley.com/doi/abs/10.1029/2021JA029298>
- Staples, F. A., Ma, Q., Kellerman, A., Rae, I. J., Sandhu, J. K., Forsyth, C., & Bortnik, J. (2023). Differentiating Between Simultaneous Loss Drivers in Earth's Outer Radiation Belt: Multi Dimensional Phase Space Density Analysis. *Accepted to Geophysical Research Letters*.
- Staples, F. A., Rae, I. J., Forsyth, C., Smith, A. R. A., Murphy, K. R., Raymer, K. M., et al. (2020). Do Statistical Models Capture the Dynamics of the Magnetopause During Sudden Magnetospheric Compressions? *Journal of Geophysical Research: Space Physics*, 125(4), e2019JA027289. <https://agupubs.onlinelibrary.wiley.com/doi/abs/10.1029/2019JA027289>
- Subbotin, D. A., & Shprits, Y. Y. (2009). Three-dimensional modeling of the radiation belts using the Versatile Electron Radiation Belt (VERB) code. *Space Weather*, 7(10).  
<https://agupubs.onlinelibrary.wiley.com/doi/abs/10.1029/2008SW000452>
- Thébault, E., Finlay, C. C., Beggan, C. D., Alken, P., Aubert, J., Barrois, O., et al. (2015). International Geomagnetic Reference Field: the 12th generation. *Earth, Planets and Space*, 67(1), 79.  
<https://doi.org/10.1186/s40623-015-0228-9>

- Tsyganenko, N. A. (1989). A magnetospheric magnetic field model with a warped tail current sheet. *Planetary and Space Science*, 37(1), 5-20.  
<https://www.sciencedirect.com/science/article/pii/0032063389900664>
- Turner, D. L., & Li, X. (2011). Using spacecraft measurements ahead of Earth in the Parker spiral to improve terrestrial space weather forecasts. *Space Weather*, 9(1).  
<https://agupubs.onlinelibrary.wiley.com/doi/abs/10.1029/2010SW000627>
- Tuszewski, M., Cayton, T. E., Ingraham, J. C., & Kippen, R. M. (2004). Bremsstrahlung effects in energetic particle detectors. *Space Weather*, 2(10).  
<https://agupubs.onlinelibrary.wiley.com/doi/abs/10.1029/2003SW000057>
- Walt, M. (1994). *Introduction to geomagnetically trapped radiation*: Cambridge University Press.
- Watt, C. E. J., Allison, H. J., Meredith, N. P., Thompson, R. L., Bentley, S. N., Rae, I. J., et al. (2019). Variability of Quasilinear Diffusion Coefficients for Plasmaspheric Hiss. *Journal of Geophysical Research: Space Physics*, 124(11), 8488-8506.  
<https://agupubs.onlinelibrary.wiley.com/doi/abs/10.1029/2018JA026401>
- Wei, L., Zhong, Q., Lin, R., Wang, J., Liu, S., & Cao, Y. (2018). Quantitative Prediction of High-Energy Electron Integral Flux at Geostationary Orbit Based on Deep Learning. *Space Weather*, 16(7), 903-916.  
<https://agupubs.onlinelibrary.wiley.com/doi/abs/10.1029/2018SW001829>
- Wong, J.-M., Meredith, N. P., Horne, R. B., Glauert, S. A., & Ross, J. P. J. (2024). New Chorus Diffusion Coefficients for Radiation Belt Modeling. *Journal of Geophysical Research: Space Physics*, 129(1), e2023JA031607.  
<https://agupubs.onlinelibrary.wiley.com/doi/abs/10.1029/2023JA031607>